ACS APPLIED ENERGY MATERIALS

www.acsaem.org Article

Cobalt Metal–Cobalt Carbide Composite Microspheres for Water Reduction Electrocatalysis

Kenta Kawashima, Kihyun Shin, Bryan R. Wygant, Jun-Hyuk Kim, Chi L. Cao, Jie Lin, Yoon Jun Son, Yang Liu, Graeme Henkelman, and C. Buddie Mullins*

Cite This: *ACS Appl. Energy Mater.* 2020, 3, 3909–3918 Read Online

ACCESS | Metrics & More | Article Recommendations | Supporting Information

ABSTRACT: Microspheres of cobalt metal–cobalt carbide (Co–Co_xC, Co_xC: Co_2C and Co_3C) composite with carbon shells were prepared via an OH^-- and Cl^--assisted polyol method and investigated for electrocatalytic activity and stability for the hydrogen evolution reaction (HER) in acidic media. From our transmission electron microscopy observations, the outermost surfaces of the as-prepared Co–Co_xC composites were primarily covered with Co_2C crystallites. Our best performing electrocatalyst exhibited superior HER activity with an overpotential of 78 mV to reach a current density of −10 mA·cm^{-2}, a Tafel slope of 87.8 mV·dec^{-1}, and 1 h of electrode durability. We show that this excellent HER performance is primarily due to the superior intrinsic activity of Co_2C, as well as the high electrical conductivity resulting from the inclusion of cobalt metal and the presence of graphitic carbon shells in and on the composite, respectively. Using both computational and experimental approaches, we determine that the carbon-rich cobalt carbide (Co_2C) phase is more favorable for the HER than the carbon-poor phase (Co_3C).

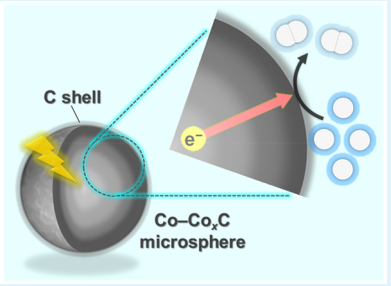

KEYWORDS: *electrocatalyst, hydrogen evolution, cobalt carbide, water splitting, polyol method*

1. INTRODUCTION

Further industrialization will rely heavily on nonrenewable fossil fuels that are being rapidly depleted, which creates a demand for an alternative energy source such as hydrogen produced via electrochemical overall water splitting using solar energy.[1] Total water splitting consists of both the hydrogen evolution reaction [HER; $2H^+(aq) + 2e^- \rightarrow H_2(g)$] and the oxygen evolution reaction [OER; $2H_2O(l) \rightarrow O_2(g) + 4H^+(aq) + 4e^-$], producing hydrogen as a renewable fuel from water. To date, researchers have reported platinum for the HER and ruthenium oxide and iridium oxide for the OER as benchmarks for electrocatalysts.[2] However, their high costs inhibit practical application. Recently, transition metal carbides, pnictides, and chalcogenides have been reported as alternative electrocatalyst materials because they are highly active, robust, and inexpensive.[3,4] Using these materials, extremely robust electrocatalysts with low HER and OER overpotentials can be designed through optimization of chemical composition and physical morphology. For example, Yu et al. reported that metallic iron and dinickel phosphides (FeP/Ni_2P) on nickel foams achieved exceptionally low overpotentials for the HER (14 mV at −10 mA·cm^{-2}) and OER (154 mV at 10 mA·cm^{-2}), substantially outperforming benchmark platinum- and ruthenium-/iridium-based electrocatalysts.[5] Moreover, the FeP/Ni_2P hybrid electrocatalysts were installed on both the cathode and anode sides in an alkaline water electrolyzer and maintained catalytic performance for 40 h at a current density of 500 mA cm^{-2} (cell voltage, 1.72 V).

Transition metal carbides, pnictides, and chalcogenides have been extensively studied for the HER over the past decade.[3,6−9] Under reductive potentials (i.e., electrochemical HER testing conditions), most of these materials demonstrate high stability and HER performance. Within this material family, transition metal carbides (as typified by Mo_2C, W_2C, and WC) may be promising, due to an electronic structure that is similar to the Pt d-band and generated from the hybridization and broadening of the transition metal d orbitals with carbon s and p orbitals.[7,10] According to a recent study,[11] the metal carbides generally exhibit higher HER activities than their parent metals. However, due to their relatively short research history, there is still room for further improving their HER performance.

Cobalt carbides (i.e., Co_3C and Co_2C) are among the most highly active electrocatalysts for the HER in both acidic and alkaline aqueous solutions.[12−15] As an example, Fan et al. synthesized nanocrystalline Co_3C embedded on vertically aligned graphene nanoribbons (GNRs) via a hot filament

Received: February 13, 2020
Accepted: March 5, 2020
Published: March 5, 2020

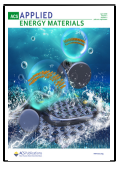

chemical vapor deposition method.[12] Because of the microporous structure of the Co_3C-GNRs and the small size of the Co_3C nanocrystals with a large number of active catalytic sites, Co_3C-GNRs showed a low overpotential (91 mV at −10 mA·cm^{-2}) in an acidic environment. In an alkaline medium, Co_2C nanoparticles synthesized through a bromide-induced wet-chemistry method demonstrated excellent HER performance with an overpotential of 181 mV at a current density of −10 mA·cm^{-2}.[14] However, further investigation is still necessary to more fully develop cobalt carbides as highly efficient HER electrocatalysts for energy conversion. So far, the Co_2C phase has not been tested as a HER electrocatalyst in an acidic medium. Additionally, the difference in intrinsic activity depending on different compositions (Co_2C vs Co_3C) has yet to be elucidated, although there are several reports about cobalt carbide HER electrocatalysts.

In this work, we report the successful improvement of cobalt carbide electrochemical HER activity in acidic media through the creation of cobalt metal (Co) and cobalt carbide (Co_xC: Co_3C and Co_2C) composite microspheres via a polyol process. Specifically, the best Co−Co_xC microsphere electrocatalyst delivered a current density of −10 mA·cm^{-2} at an overpotential of 78 mV. Using both computational and experimental results, we find that Co_2C has higher intrinsic activity for hydrogen evolution compared with Co_3C. Building upon these findings, the use of similar composites may be applicable to other transition metal carbides, paving the way to further improvements to their HER activity.

2. EXPERIMENTAL SECTION

2.1. Materials. Cobalt acetate tetrahydrate (98+%, Acros Organics), tetraethylene glycol (99%, Sigma-Aldrich), KOH (86.4%, Fisher Scientific), KCl (99.5%, Fisher Scientific), ethyl alcohol (Pharmco-Aaper), 1-propanol (>99 wt %, Fisher Scientific), Nafion perfluorinated ion-exchange resin solution (5 wt % solution in lower aliphatic alcohols/water mixture, Sigma-Aldrich), carbon black (CB, Hanwha Chemical), and H_2SO_4 (96.2 wt %, Fisher Scientific) were used for synthetic and electrochemical experiments. Eighteen MΩ ultrapure water was used for all solutions.

2.2. Polyol Synthesis. Co-based products were synthesized via a polyol process, which is a modification of a previously reported procedure.[16] Cobalt acetate tetrahydrate (precursor, 0.50 g), tetraethylene glycol (solvent. carbon source, and reducing agent, 50 mL), and KCl and KOH (0.10, 0.25, and 0.50 M, 1:1 molar ratio) were placed in a three-neck flask. Salt concentrations were varied to control the resultant phase composition. As seen in Supporting Information Figure S1, the as-prepared mixture was heated at ∼240 °C for 15 min under reflux, with magnetic stirring (1150 rpm) and N_2 gas flow to remove most of the ambient atmosphere. The as-obtained Co-based products were magnetically separated from the supernatant and byproducts (i.e., cubic CoO), rinsed with ethyl alcohol 3−5 times, and then dried under vacuum at room temperature to inhibit surface oxidation.

2.3. Characterization. The resultant crystal phases were identified using a Rigaku Miniflex 600 powder X-ray diffractometer (XRD, Rigaku, Japan) with Cu Kα radiation (λ = 1.5406 Å). The surface chemical compositions of the as-obtained Co-based products were examined using an X-ray photoelectron spectrometer (XPS) model Axis-Ultra DLD (Kratos Analytical, USA) equipped with a monochromatic Al Kα_1 X-ray source. The morphology and size of the as-obtained Co-based products were investigated by a Quanta 650 environmental scanning electron microscope (ESEM, FEI, USA) with an energy dispersive X-ray spectrometer (EDX). EDX line scans were performed using a 30 kV acceleration voltage. The surfaces of the as-obtained Co-based products were observed by a field emission transmission electron microscope (FETEM, JEM-2010F, JEOL, Japan) at an accelerating voltage of 200 kV.

2.4. Electrode Preparation. The Co-based material thin films with carbon black as an additive (Co-based material/CB) were fabricated on glassy carbon (GC) electrodes (0.19625 cm^2) via a drop-casting method. First, an ink of Co-based material/CB in a 4:1 weight ratio was prepared by ultrasonically dispersing 15.1 mg of Co-based material and 3.8 mg of CB in a 1.0 mL solution (0.75 mL of deionized water and 0.25 mL of 1-propanol) for ∼1 h. Subsequently, 13 μL of the as-prepared ink and 12 μL of 0.1 wt % Nafion solution were cast on the GC electrode and dried in air at room temperature. Here, the Co-based material loading for all measurements was ∼1 mg·cm^{-2}.

2.5. Electrochemical Measurements. To evaluate HER performance, electrochemical measurements of the Co-based material/CB-modified GC electrodes were conducted in a N_2-purged 0.5 M H_2SO_4 aqueous solution (pH ∼ 0.3) using a computer-based electrochemical workstation with a standard three-electrode system [working electrode, Co-based material/CB/GC electrode; counter electrode, graphite (C) rod; reference electrode, Ag/AgCl (saturated KCl)] at room temperature. Linear sweep voltammetry (LSV) was performed with a scan rate of 5 mV·s^{-1} using a rotating disk electrode technique (1600 rpm). All of the electrochemical measurements were compensated by 80% *iR* drop.

To understand the effect of surface area on HER performance, the roughness factor (RF) was also calculated [RF = electrochemically active surface area (ECSA)/geometric electrode surface area (GESA)]. Here, the ECSA was estimated from the electrochemical double-layer capacitance (C_{dl}) of the electrocatalytic surface [ECSA = C_{dl}/C_s, C_s being the specific capacitance (the capacitance of an atomically smooth planar surface of the material per unit area), C_s = 22 μF·cm^{-2}].[12,17] Cyclic voltammograms (CVs) with different scan rates were taken in a potential window without faradaic processes (−0.11 to −0.01 $V_{Ag/AgCl}$) to obtain C_{dl} from the scan-rate dependence of double-layer charging [$\Delta j/2 = (j_a - j_c)/2$]. The potentials measured relative to Ag/AgCl were converted to the reversible hydrogen electrode (RHE) scale via the Nernst equation [$V_{RHE} = V_{Ag/AgCl} + 0.0591\text{pH} + V^{\circ}_{Ag/AgCl}$; $V^{\circ}_{Ag/AgCl}$(saturated KCl) = 0.1976 V at 25 °C].

2.6. Computational Details. Generalized gradient approximation (GGA) level spin-polarized density functional theory (DFT) calculations were performed with the Vienna ab initio simulation package using a plane wave basis set with a cutoff energy of 400 eV. The revised Perdew−Burke−Ernzerhof functional (RPBE) was used to describe electron exchange and correlation.[18−20] The Brillouin zone was sampled with a 2 × 2 × 1 *k*-point mesh following the Monkhorst−Pack scheme. The convergence criteria for electronic and geometrical optimization were 10^{-5} eV and 0.01 eV·Å^{-1}, respectively. We made a set of Co_2C (space group *Pnnm*) and Co_3C (space group *Pnma*) slab models with low Miller indices; {100}, {110}, and {111}. The surfaces were expanded into a 2 × 2 super cell, with the exception of Co_3C (101), (110), and (010) to 1 × 2, (111) to 1 × 1, and (011) to 2 × 1, which were selected to have a similar H* coverage. All surfaces had a 20 Å vacuum gap in the *z*-direction. The atoms in the lower half of each slab were fixed in their bulk positions. The Gibbs free energy (ΔG) was calculated from the following equation:

$$\Delta G \text{ (at } U = 0 \text{ V)} = \Delta E - \Delta E_{ZPE} - T\Delta S - neU$$

where ΔE is the reaction energy, ΔE_{ZPE} is the zero-point energy correction, ΔS is the difference in entropy, and U is the applied potential. The chemical potential of the solvated proton and electron pair ($H^+ + e^-$) at standard conditions (p_{H_2} = 1 bar, a_{H^+} = 1, T = 298.15 K) is calculated as 0.5 $\mu^0_{H_2(g)} - eU$ by assuming equilibrium with the standard hydrogen electrode (SHE).[21,22] The transport properties including the electrical conductivity were calculated using BoltzTrap2 based on semiclassical Boltzmann theory under a constant relaxation time approximation.[23]

https://dx.doi.org/10.1021/acsaem.0c00321
ACS Appl. Energy Mater. 2020, 3, 3909−3918

3. RESULTS AND DISCUSSION

3.1. Characterization of Cobalt-Based Materials. To examine the effect of KCl−KOH concentration (0.10−0.50 M) on the synthesis of the Co-based products, the resultant phase was identified with XRD. Figure 1 shows the XRD patterns of the as-synthesized Co-based products in color (Co metal or Co−Co_xC) as compared to reference patterns in gray. At 0.10 M KCl−KOH, the diffraction pattern is identified as cubic Co without any impurities. Cubic Co, orthorhombic Co_3C [space group *Pbnm* (62)], and orthorhombic Co_2C [space group *Pmnn* (58)] were formed at 0.25 and 0.50 M [since the Co_3C crystal structures with the space groups of *Pbnm* and *Pnma* have the same space-group number (62), these two crystal structures are identical]. Interestingly, the carbon content in the product increases (i.e., Co → Co_3C → Co_2C) with an increase in KCl−KOH concentration, as the degree of carbidization is controlled by the OH^- concentration.[16] From the XRD results, 0.25 and 0.50 M were found to be appropriate KCl−KOH concentrations for forming a Co metal and Co carbide composite. The XRD quantitative analysis results of 0.25 and 0.50 M are also available in Figure S2.

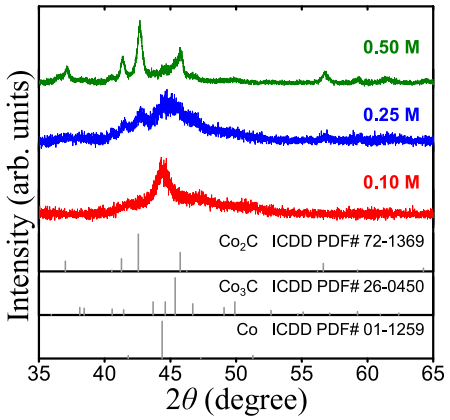

Figure 1. XRD patterns of the Co-based particles synthesized by a polyol process with different KCl−KOH concentrations (0.10−0.50 M).

To investigate surface chemical composition and states, XPS analysis of the composites was carried out. The Co $2p_{3/2}$, C 1s, and O 1s XPS core-level spectra are shown in Figures 2 and S3. The Co $2p_{3/2}$ spectra (Figure 2, blue) were deconvoluted into three doublets assignable to Co^0 (near 778.5 eV), Co^{2+} (near 780.5 eV), and satellites (at around 786 eV).[24−26] According to the previous reports regarding the Co carbides,[25,26] Co^0 and Co^{2+} species might be derived from Co carbide and Co oxide/hydroxide, respectively. The C 1s spectra appear to consist of four peaks centered at ∼285.0 eV for C−C bonds (C_1), ∼286.6 eV for C−O bonds (C_2), ∼288.6 eV for C═O bonds (C_3), and ∼282.8 eV for C−Co bonds (C_4) in Co_2C/Co_3C species (Figure 2, green).[25−27] In the O 1s spectra (Figure S2), the three components at around 529.6, 531.3, and 532.4 eV can be assigned to O−Co−O bonds (O_1), Co−OH bonds (O_2), and physi-/chemisorbed H_2O or C═O and O−C═O bonds (O_3), respectively,[28,29] indicating that all of the product surfaces might be partially oxidized during the synthesis and/or by ambient air exposure. Together, the XPS spectra of our samples show that the surfaces of the 0.25 and 0.50 M composites consist primarily of Co carbide, Co oxide, and $Co(OH)_2$, as well as some adsorbed organic impurities and water.

After confirming the composition of the as-synthesized Co-based particles, the influence of the KCl−KOH concentration on their sizes and morphologies were inspected with SEM (Figure 3). At 0.10 M, primarily rough microsphere-like nanoparticle assemblies (i.e., microspheres) were formed

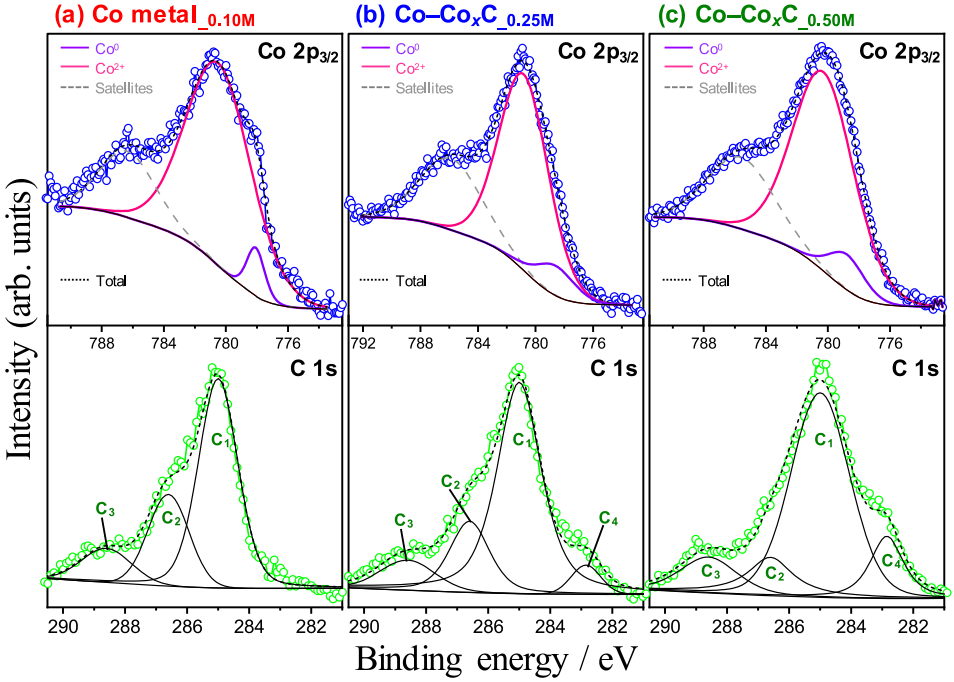

Figure 2. Co 2p and C 1s XPS core-level spectra of the Co-based particles synthesized by a polyol process with different KCl−KOH concentrations: (a) 0.10, (b) 0.25, and (c) 0.50 M.

https://dx.doi.org/10.1021/acsaem.0c00321
ACS Appl. Energy Mater. 2020, 3, 3909−3918

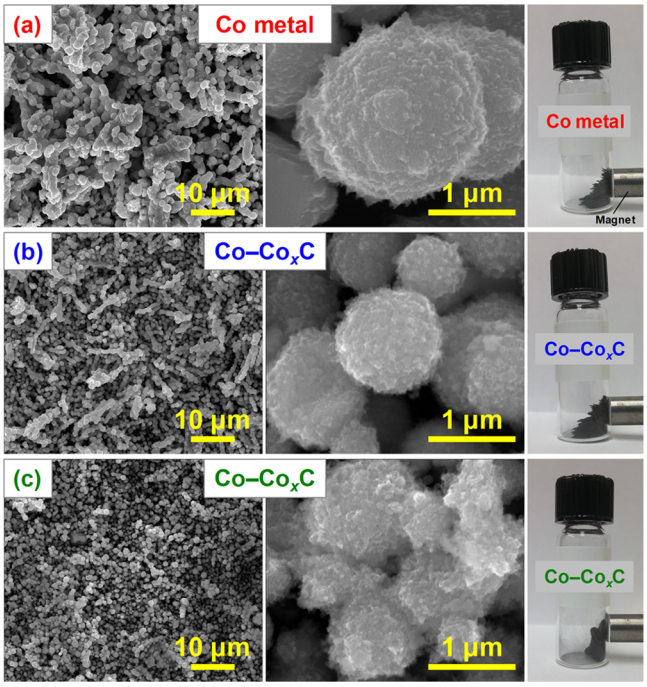

Figure 3. SEM images (left side and center columns) and digital photographs (right column) of the Co-based particles synthesized by a polyol process with different KCl–KOH concentrations: (a) 0.10, (b) 0.25, and (c) 0.50 M.

(Figure 3a). At 0.25 and 0.50 M, the smaller particles of the same morphology were seen along with minor nanorod assembles (Figures 3b,c). Microchain (chain-like or necklace-like morphology consisting of several microspheres) formation was confirmed in all of the as-obtained samples, and the number of the microchains observed decreased as the KCl–KOH concentration increased. Additionally, the dominant microsphere sizes decreased with increasing KCl–KOH concentration: 1.6 ± 0.3 μm for 0.10 M, 1.1 ± 0.2 μm for 0.25 M, and 1.0 ± 0.2 μm for 0.50 M. These morphological differences are important and will be discussed in more detail later in this work. Finally, as demonstrated in Figure 3, all of the Co-based products also exhibited magnetic properties, which indicate the presence of cobalt metal and/or carbide in our samples.[16,30]

EDX elemental mapping images of 0.25 and 0.50 M samples on Si wafer substrates are shown in Figure S4. Co (blue) and C (green) elements were distributed throughout the particles obtained at 0.25 and 0.50 M. Weak O (red) signals were also observed, which may correspond to the surface oxidation of the as-obtained microspheres. Additionally, to better understand the spatial distribution of the different elements in the Co–Co$_x$C composites synthesized at 0.25 and 0.50 M KCl–KOH concentrations, we measured the EDX line-scan elemental profiles across the middle of the as-obtained particles (Figure 4). The EDX results for both conditions show Co enrichment in the center of the particles and C enrichment at the surface. Both EDX line and mapping analysis again showed the presence of O, additional evidence of surface oxidation. The 0.50 M sample showed the highest degree of carbon enrichment at the surface, which may be due to a greater degree of carbidization at 0.50 M than at 0.25 M (see Figure 1). Note that the resultant microspheres are mixtures of Co

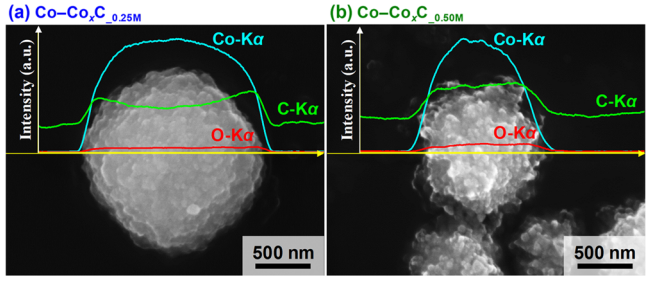

Figure 4. EDX line-scanned elemental profiles of the Co-based particles synthesized by a polyol process with different KCl–KOH concentrations: (a) 0.25 and (b) 0.50 M. The sample powders were loaded onto carbon tape supports.

and Co$_x$C with the Co$_x$C/Co ratio presumably increasing from the center to the outside.

To further examine the morphological and crystallographic details for the 0.25 and 0.50 M samples, we conducted TEM and high-resolution TEM (HRTEM) measurements of the as-synthesized large microspheres (main products) and small particles (minor products), as seen in Figures S5 and 5. Here, a

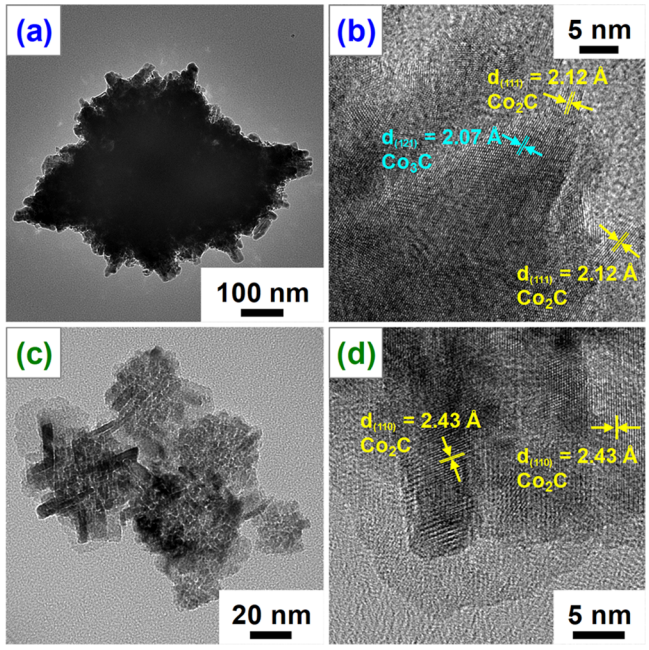

Figure 5. TEM and HRTEM images of the Co-based particles synthesized by a polyol process with different KCl–KOH concentrations: (a and b) 0.25 and (c and d) 0.50 M.

layer composed of both graphitic and amorphous carbon appeared in both the 0.25 and 0.50 M microspheres (Figure S5a,b). Notably, graphitic carbon is known to be effective for improving the electrical conductivity and (electro)chemical stability.[12,31−36] In addition to the carbon layer, we also observe the presence of smaller nanocrystals at and within the surface of the larger microsphere. On the basis of these TEM images, the previously shown SEM images, and the broad XRD peaks, we have determined that the microspheres are likely aggregations of various smaller nanocrystals. The thickness of the microparticle aggregates prevents lattice analysis in the interior of the particles, however. Thus, to better confirm the crystallographic phases present in the samples, we instead

https://dx.doi.org/10.1021/acsaem.0c00321
ACS Appl. Energy Mater. 2020, 3, 3909−3918

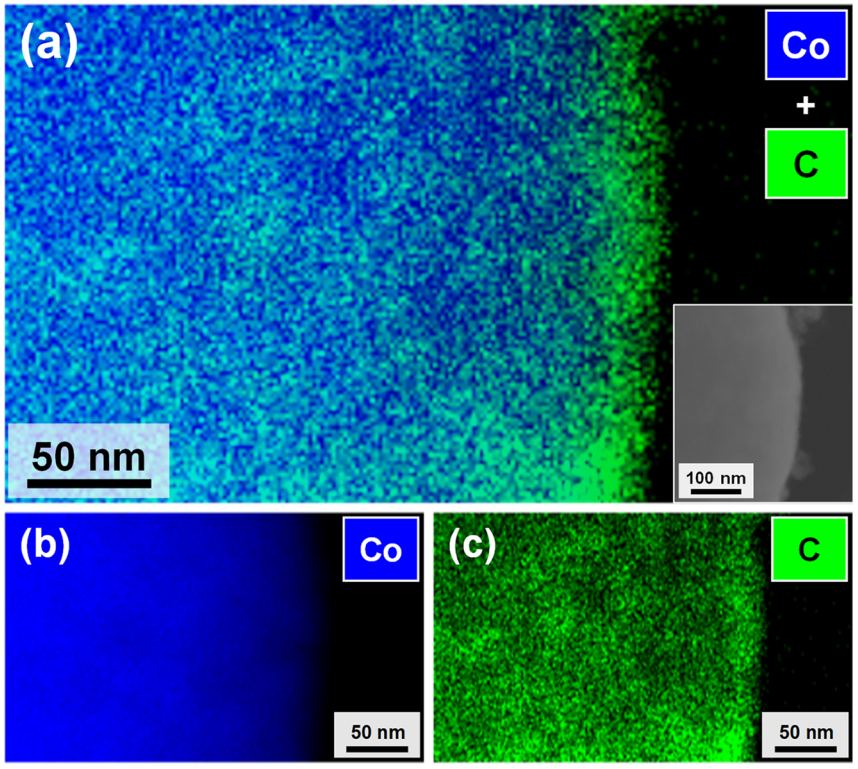

Figure 6. (a–c) STEM-EDX elemental mapping images and (bottom right inset of Figure 6a) dark-field STEM image of selected area from the Co-based particle synthesized by a polyol process with the KCl–KOH concentration at 0.25 M.

studied smaller particles which are representative of those within the bulk microparticles, as shown in Figure S5c–f; the HRTEM images in Figure 5b,d show lattice spacings from these nanocrystals. In images from the 0.25 M composite (Figures 5b and S6), we can observe both orthorhombic Co_2C and Co_3C at and near the surface of the smaller nanocrystals. Especially, as shown in Figure 5b, crystalline Co_3C was covered with Co_2C crystallites. For the 0.50 M sample, nanorod assemblies were observed, with an interplanar distance of 2.43 Å (Figures 5d and S6), which corresponds to the (110) plane in orthorhombic Co_2C. These measurements confirm our earlier XRD and XPS results and clearly show the presence of crystalline Co_2C at the outermost surface of our Co–Co_xC composite electrocatalysts.

Due to the lower sensitivity of SEM-based EDX analysis, a result of the thicker samples analyzed, we performed scanning TEM (STEM)-EDX elemental mapping analysis on a representative microsphere sample (0.25 M) to further confirm the existence of a carbon-rich shell. Figure 6 clearly indicates that the microsphere sample possesses the Co–Co_xC@C core@shell structure, which may be advantageous with respect to electrical conductivity and (electro)chemical stability.[12,31−35] In previous studies using the polyol method,[16,37,38] similar graphitic carbon layers on cobalt carbide particles have also been reported. Additional data such as the corresponding O elemental mapping image and STEM-EDX spectra are also available in the Supporting Information (Figure S7).

On the basis of these results as well as previous reports,[16,37−39] we briefly present a possible mechanism for the crystal phase formation and the morphological development of the Co metal and Co–Co_xC microspheres in the OH^-- and Cl^--assisted polyol process. In this synthesis, there are two competing processes, (i) the diffusion of C atoms into the Co metal structure associated with the surface reconstruction (i.e., carbidization) and (ii) Co metal nucleation and particle growth.[16,38] In order to control these two events, it is important to regulate the concentration of OH^- ions in solution. Increasing the [OH^-] increases the amount of capping agent produced (glycolate ions) and lowers the distillation temperature of the solvent (tetraethylene glycol), which together slow the growth rate and accelerate carbidization.[38] Additionally, Cl^- ions coordinate to the Co nuclei and inhibit aggregation.[39] Accordingly, the growth rate of Co metal was too fast at 0.10 M KCl–KOH, and complete diffusion of C atoms did not occur; this resulted in the formation of Co metal microspheres of a relatively large size (1.6 ± 0.3 μm). On the other hand, the 0.25 and 0.50 M samples with mixed-phase Co–Co_xC had smaller sizes (0.25 M, 1.1 ± 0.2 μm; 0.50 M, 1.0 ± 0.2 μm) than the 0.10 M Co metal sample because the addition of OH^- ions suppressed the particle growth and increased the carbidization rate.

Furthermore, on the basis of the EDX line-scan analysis (Figure 4), the 0.25 and 0.50 M microspheres appear to have gradations in composition. To explain this observation, we propose the following mechanism using the 0.25 M sample as a representative example. In the primary step of microsphere growth, a large quantity of homogeneous Co nuclei was generated and dispersed in the solvent. Due to the high total surface area of the Co nuclei at this step, the capping agent was unable to effectively passivate all of the nuclei. Thus, an aggregate Co metal phase was produced as the reaction progressed and the nuclei formed polycrystalline agglomerates, which minimized the overall surface free energy as the surface area-to-volume for the aggregates decreased. Simultaneously, the concentration of the Co-based solute decreased, thereby lowering the nucleation and particle growth rates. After this

https://dx.doi.org/10.1021/acsaem.0c00321
ACS Appl. Energy Mater. 2020, 3, 3909−3918

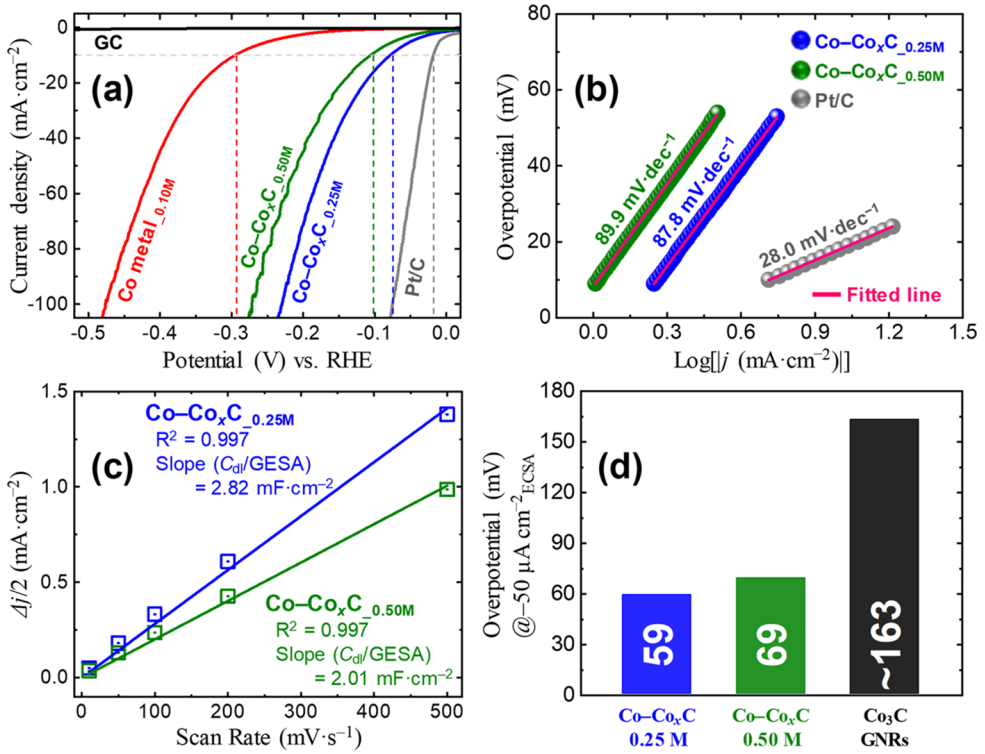

Figure 7. (a) LSV curves of the Co-based material/CB and Pt/C electrocatalysts in an acidic aqueous solution (fourth sweeps). (b) Tafel plots of the Co−Co_xC/CB and Pt/C electrocatalysts. (c) Double-layer capacitances (C_{dl}) of the Co−Co_xC/CB electrocatalysts at a potential of −0.06 $V_{Ag/AgCl}$. (d) HER overpotential comparison (based on ECSA) for Co−Co_xC/CB hybrids (this work) vs nanocrystalline Co_3C-GNRs (data from ref 12).

point, the capping agent was able to efficiently bind once more and accelerate the carbidization process, producing predominately Co_2C and Co_3C phases. When the particles grew to be ~1 μm, the reduction of the capping agent produced the graphitic layers observed in the TEM images (Figure S5a), impeding further crystal growth.[37] Consequently, the Co_xC/Co ratio would be expected to increase going from the center to the outside of the Co−Co_xC microspheres; the innermost aggregated Co particles near the microparticle core either formed and aggregated prior to carbidization, or were protected by the Co particles at the surface from subsequent carbidization (see Figure 4). In addition to the Co−Co_xC composite, cubic CoO was also formed as a byproduct in all of our experiments (see Figure S1c). Cobalt oxide is thermodynamically more stable than cobalt carbide,[40,41] and thus any O-containing impurities could produce CoO, which would not participate further in the carbidization process. We therefore postulate that the extent of CoO formation may also be a parameter which influences the carbidization degree of the resultant sample.

3.2. Electrochemical Hydrogen Evolution Reaction Performance. To test the electrocatalytic hydrogen production activity of the composites, HER LSV was first performed using CB/GC electrodes loaded with the Co metal and Co−Co_xC microspheres and tested in acidic environments (Figure 7). The HER experimental results are shown in Figure 7a, and we found that the Co metal sample (0.10 M) exhibited the largest HER overpotential on the basis of GCSA at 10 mA·cm^{-2} (η_{geo} = 295 mV). Also, due to the low chemical stability of Co metal in acidic media,[42] the 0.10 M sample underwent continual dissolution into the electrolyte during HER testing (see Figure S8). The 0.25 M Co−Co_xC sample demonstrated a lower overpotential (η_{geo} = 78 mV) than the Co−Co_xC sample at 0.50 M (η_{geo} = 106 mV), likely due to its higher Co metal content (see Figure S2) resulting in subsequently higher electrical conductivity (i.e., total film conductivity), which will be discussed in detail later in this work, as well as a larger surface area (see Figure S9). As expected, the commercial Pt/C showed the lowest overpotential (η_{geo} = 18 mV). To further explore the HER performance of the 0.25 and 0.50 M Co−Co_xC and Pt/C samples, we calculated the Tafel slopes of all materials using the Tafel equation [$\eta = b \log(|j|) + a$], where η is the overpotential, b is the Tafel slope, and j is the current density, respectively (Figure 7b). The as-obtained Tafel slopes are in the following sequence: 0.50 M Co−Co_xC (89.9 mV·dec^{-1}) > 0.25 M Co−Co_xC (87.8 mV·dec^{-1}) > Pt/C (28.0 mV·dec^{-1}).

To more deeply probe the intrinsic HER activity for each Co−Co_xC sample, we determined the ECSA using measured values of C_{dl} (Figures 7c and S9) and calculated an overpotential from current density normalized by the ECSA (mA·cm$^{-2}{}_{ECSA}$). Figure 7d shows the ECSA-normalized overpotential (η_{ECSA}) of the 0.25 and 0.50 M samples, and we have also included the same overpotential for previously reported Co_3C-graphene nanoribbons (GNRs); doing so allows us to investigate the impact of the different phases (i.e., Co_2C vs Co_3C) on the HER intrinsic activity. Our Co−Co_xC samples, which have Co_2C crystallites on their outermost surfaces (see Figure 5b,d), show much higher HER intrinsic activities [η_{ECSA} = 59 (0.25 M) and 69 (0.50 M) mV] than the Co_3C-GNRs (η_{ECSA} = ~163 mV). Therefore, we find it likely that Co_2C has a higher HER intrinsic activity compared to Co_3C. Additional support for this determination comes from calculations of the Gibbs free energy (ΔG_{H^*}) of a hydrogen

https://dx.doi.org/10.1021/acsaem.0c00321
ACS Appl. Energy Mater. 2020, 3, 3909−3918

atom adsorbed on the catalyst surface (H*, where * denotes a site on the surface).[43] Figure 8 shows the calculated H*

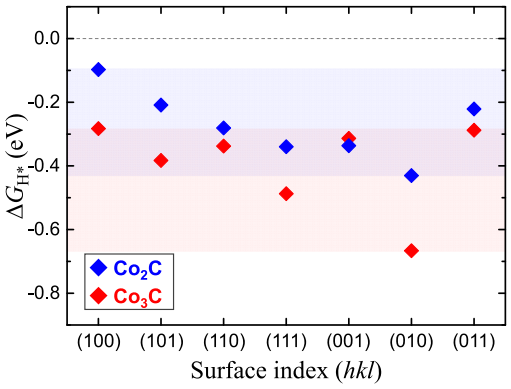

Figure 8. DFT-calculated H* binding energies of Co_2C (blue) and Co_3C (red) for different crystal facets.

binding energies on different crystal facets of both Co_2C and Co_3C, and additional details about the computational models are available in Figure S10. For almost all crystal facets, Co_2C has more positive H* binding energies (closer to 0 eV) when compared to Co_3C, which implies that Co_2C has a better H* binding strength that leads to more efficient HER electrocatalysis. It is clear from the above experimental and computational results that Co_2C is an intrinsically more active HER catalyst as compared to Co_3C.

Additionally, the 0.25 M sample exhibited a slightly lower ECSA-based overpotential than the 0.50 M sample. This might be because a relatively large amount of conductive Co metal (Figure S2) on and in the 0.25 M sample could increase the total film conductivity and facilitate electron access at surface-active sites. As evidence of the improved electrical conductivity, the total resistance of the HER testing cells were measured using a potentiostat for the 0.25 and 0.50 M samples. The measured total resistance for the 0.50 M system (11 Ω) is higher than that of the 0.25 M system (8.7 Ω). There were no differences in electrode placement or electrolyte between tests, and thus it is most likely that the difference in the resistances is due to differences in the conductivity of the 0.25 and 0.50 M Co−Co_xC catalyst films themselves. Hence, the catalyst film fabricated using the 0.25 M sample has a higher electrical conductivity compared with the catalyst film using the 0.50 M sample. To further support these data, the electrical conductivity of each material (i.e., Co_2C, Co_3C, and Co) was determined using a previous report and our computational results.[44] As shown in Table S1, Co_2C (5.30×10^{10} S·cm^{-1}) and Co_3C (2.49×10^{10} S·cm^{-1}) show similar electrical conductivity. Just as expected, Co metal has a much higher conductivity (1.668×10^{11} S·cm^{-1}) than Co_2C and Co_3C. Accordingly, the Co metal-rich 0.25 M sample could have a lager total film conductivity than the Co metal-poor 0.50 sample.

Due to the observed electrochemical instability of the 0.10 M sample, we tested the stability of the champion 0.25 M Co−Co_xC/CB/GC electrode using chronoamperometry at constant potentials of −0.32 and −0.82 mV vs RHE. As seen in Figure S11, a moderately high current density (−0.32 mV vs RHE) was observed for 1 h, but gradually decreased as the experiment progressed (Figure S11a). At −0.82 mV vs RHE, a similar behavior was also observed (Figure S11b). To determine what caused the loss in current density, we performed SEM-EDX analysis of the Co−Co_xC/CB film before and after the 1 h chemical stability test (the experimental details are available in the Supporting Information). After the chemical stability test, most of the Co−Co_xC microspheres and microchains remained (Figures S12 and S13), indicating that the Co−Co_xC is somewhat chemically stable, but some of the Co−Co_xC microspheres and microchains were chemically damaged: the centers of the Co−Co_xC particles were selectively etched out (Figure S14). As previously stated, Co metal is chemically unstable in acidic solutions,[42] the selective dissolution of the Co metal-rich core [$Co(s) + H_2SO_4(aq) \rightarrow CoSO_4(aq) + H_2(g)$; see Figure S15a] might have happened because some of the Co−Co_xC particles might have incomplete coverage of Co carbides on the Co metal surface (Figure S15b). Moreover, since the as-synthesized Co−Co_xC particle is an aggregate of Co metal and carbide nanoparticles, the selective dissolution of the Co metal nanoparticles might cause the structural destruction of Co carbide-rich shells and following physical detachment of Co carbide nanoparticles from substrates, resulting in the shapes as shown in Figure S14. These SEM results (Figure S14) suggest that instability observed in the Co−Co_xC/CB/GC system is chemical and mechanical and is primarily caused by (i) selective dissolution of Co metal-rich cores and (ii) detachment of Co carbide nanoparticles from the GC substrate, which decrease the overall conductivity and the number of HER active sites, respectively. A study to form the perfect Co@Co_xC core@shell structure (without Co metal exposure) is ongoing to improve the chemical stability of the electrocatalyst film. Additionally, these SEM results can also confirm that the carbon shells (Figures S5a and 6) are ionically conductive, providing the direct contacts between the Co_2C-dominant surfaces and the electrolyte. In other words, active sites for the HER are the Co_2C-dominant surfaces rather than the carbon shells.

Thus far, several studies have reported the HER performance of Co_3C-based electrodes in acidic and alkaline environments;[12,13,15] however, Co_2C has been lightly studied (there is only one report in an alkaline media).[14] To validate the effectiveness of our strategy, we compared the HER performance of our Co−Co_xC catalysts with those of other reported cobalt carbide-based catalysts according to the overpotential based on GESA at 10 mA·cm^{-2}; the details are listed in Table S2. The HER performance of our best sample (0.25 M) is superior to several recently reported results.[12−15] For comparison, Co_3C-GNRs showed a GESA-based overpotential of 91 mV, which is currently the lowest overpotential among the cobalt carbide-based catalysts. The calculated RF of Co_3C-GNRs (981.8) is ∼8 times higher than that of our best sample (128.2), and nevertheless, our best sample has a higher HER activity (η_{geo} = 78 mV) compared to Co_3C-GNRs. As previously mentioned, we attribute the superior HER performance of our best performing Co−Co_xC catalyst as likely due to the presence of (i) intrinsically active Co_2C, (ii) conductive Co metal, and a (iii) conductive C shell. These results suggest that synthesis of metal−metal-carbide composites via a polyol method can yield improved HER performance, and we predict this strategy can be applied to other transition metal/bimetal carbides (e.g., molybdenum carbide,[45,46] tungsten carbide,[46] cobalt−molybdenum carbide,[47,48] and so forth) as well.

https://dx.doi.org/10.1021/acsaem.0c00321
ACS Appl. Energy Mater. 2020, 3, 3909−3918

4. CONCLUSIONS

In summary, Co−Co_xC composite microspheres encapsulated in carbon shells were grown through a OH^-- and Cl^--assisted polyol process. The best sample, prepared at 0.25 M KCl−KOH concentration, demonstrated considerably enhanced HER activity (η_{geo} = 78 mV), due to high electrical conductivity resulting from the incorporation of both Co metal and a graphitic C shell, as well as the existence of Co_2C surface active species. A long-term chronoamperometric test showed the best performing Co−Co_xC composite sample could stably evolve hydrogen for 1 h. However, its chemical stability still needs to be improved. Importantly, the theoretical results revealed that the orthorhombic Co_2C phase is intrinsically more active toward the HER and has a slightly higher electrical conductivity compared to the orthorhombic Co_3C phase. These findings clearly demonstrate the importance of controlling the crystalline phase and electrical conductivity for tuning the electrocatalytic properties and provide an explanation for the impressive HER performance exhibited by this material.

■ ASSOCIATED CONTENT

Supporting Information

The Supporting Information is available free of charge at https://pubs.acs.org/doi/10.1021/acsaem.0c00321.

Experimental details, schematic illustrations, XRD pattern, XRD quantitative analysis results, O 1s XPS results, EDX elemental mapping images, additional TEM, HRTEM, and STEM-EDX results, LSVs, CVs, DFT-calculated electrical conductivities and resistivities, chronoamperometric curves, SEM and EDX elemental mapping images, and comparison of this work with previous reports (PDF)

■ AUTHOR INFORMATION

Corresponding Author

C. Buddie Mullins − *Department of Chemistry, John J. McKetta Department of Chemical Engineering, and Center for Electrochemistry, The University of Texas at Austin, Austin, Texas 78712, United States;* orcid.org/0000-0003-1030-4801; Email: mullins@che.utexas.edu

Authors

Kenta Kawashima − *Department of Chemistry, The University of Texas at Austin, Austin, Texas 78712, United States;* orcid.org/0000-0001-7318-6115

Kihyun Shin − *Department of Chemistry and Oden Institute for Computational Engineering and Sciences, The University of Texas at Austin, Austin, Texas 78712, United States;* orcid.org/0000-0002-1748-8773

Bryan R. Wygant − *Department of Chemistry, The University of Texas at Austin, Austin, Texas 78712, United States*

Jun-Hyuk Kim − *John J. McKetta Department of Chemical Engineering, The University of Texas at Austin, Austin, Texas 78712, United States*

Chi L. Cao − *John J. McKetta Department of Chemical Engineering, The University of Texas at Austin, Austin, Texas 78712, United States*

Jie Lin − *John J. McKetta Department of Chemical Engineering, The University of Texas at Austin, Austin, Texas 78712, United States; College of Materials, Xiamen University, Xiamen, Fujian 361005, China;* orcid.org/0000-0002-1281-9713

Yoon Jun Son − *John J. McKetta Department of Chemical Engineering, The University of Texas at Austin, Austin, Texas 78712, United States*

Yang Liu − *John J. McKetta Department of Chemical Engineering, The University of Texas at Austin, Austin, Texas 78712, United States; College of Chemistry and Chemical Engineering, Central South University, Changsha, Hunan 410083, China;* orcid.org/0000-0002-7240-1546

Graeme Henkelman − *Department of Chemistry and Oden Institute for Computational Engineering and Sciences, The University of Texas at Austin, Austin, Texas 78712, United States;* orcid.org/0000-0002-0336-7153

Complete contact information is available at: https://pubs.acs.org/10.1021/acsaem.0c00321

Notes

The authors declare no competing financial interest.

■ ACKNOWLEDGMENTS

We gratefully acknowledge the National Science Foundation via Grant CHE-1664941 (C.B.M.) for support of the experimental portion of this work and the U.S. Department of Energy Basic Energy Sciences Grant DE-SC0010576 (G.H.) for the computational portion of the study. We also acknowledge the Welch Foundation for their generous support through Grants F-1436 (C.B.M) and F-1841 (G.H.). Computational resources were provided by the Texas Advanced Computing Center and the National Energy Research Scientific Computing Center. Additionally, we thank Dr. Hugo Celio for his kind assistance in XPS measurements. Discussions and comments on electrochemical measurements from Dr. Oluwaniyi Mabayoje are gratefully acknowledged.

■ REFERENCES

(1) Montoya, J. H.; Seitz, L. C.; Chakthranont, P.; Vojvodic, A.; Jaramillo, T. F.; Nørskov, J. K. Materials for solar fuels and chemicals. *Nat. Mater.* **2017**, *16* (1), 70−81.

(2) McCrory, C. C.; Jung, S.; Ferrer, I. M.; Chatman, S. M.; Peters, J. C.; Jaramillo, T. F. Benchmarking hydrogen evolving reaction and oxygen evolving reaction electrocatalysts for solar water splitting devices. *J. Am. Chem. Soc.* **2015**, *137* (13), 4347−4357.

(3) Zeng, M.; Li, Y. Recent advances in heterogeneous electrocatalysts for the hydrogen evolution reaction. *J. Mater. Chem. A* **2015**, *3*, 14942−14962.

(4) Wygant, B. R.; Kawashima, K.; Mullins, C. B. Catalyst or precatalyst? The effect of oxidation on transition metal carbide, pnictide, and chalcogenide oxygen evolution catalysts. *ACS Energy Lett.* **2018**, *3* (12), 2956−2966.

(5) Yu, F.; Zhou, H.; Huang, Y.; Sun, J.; Qin, F.; Bao, J.; Goddard, W. A., III; Chen, S.; Ren, Z. High-performance bifunctional porous non-noble metal phosphide catalyst for overall water splitting. *Nat. Commun.* **2018**, *9* (1), 2551.

(6) Vesborg, P. C.; Seger, B.; Chorkendorff, I. B. Recent development in hydrogen evolution reaction catalysts and their practical implementation. *J. Phys. Chem. Lett.* **2015**, *6* (6), 951−957.

(7) Chen, W. F.; Muckerman, J. T.; Fujita, E. Recent developments in transition metal carbides and nitrides as hydrogen evolution electrocatalysts. *Chem. Commun.* **2013**, *49* (79), 8896−8909.

(8) You, B.; Sun, Y. Chalcogenide and phosphide solid-state electrocatalysts for hydrogen generation. *ChemPlusChem* **2016**, *81* (10), 1045−1055.

(9) Yang, W.; Rehman, S.; Chu, X.; Hou, Y.; Gao, S. Transition metal (Fe, Co and Ni) carbide and nitride nanomaterials: structure,

chemical synthesis and applications. *ChemNanoMat* **2015**, *1* (6), 376−398.
(10) Kitchin, J. R.; Nørskov, J. K.; Barteau, M. A.; Chen, J. G. Trends in the chemical properties of early transition metal carbide surfaces: a density functional study. *Catal. Today* **2005**, *105* (1), 66−73.
(11) Michalsky, R.; Zhang, Y. J.; Peterson, A. A. Trends in the hydrogen evolution activity of metal carbide catalysts. *ACS Catal.* **2014**, *4* (5), 1274−1278.
(12) Fan, X.; Peng, Z.; Ye, R.; Zhou, H.; Guo, X. M_3C (M: Fe, Co, Ni) nanocrystals encased in graphene nanoribbons: An active and stable bifunctional electrocatalyst for oxygen reduction and hydrogen evolution reactions. *ACS Nano* **2015**, *9* (7), 7407−7418.
(13) Ma, X. X.; He, X. Q.; Asefa, T. Hierarchically porous Co_3C/Co-NC/G modified graphitic carbon: A trifunctional corrosion-resistant electrode for oxygen reduction, hydrogen evolution and oxygen evolution reactions. *Electrochim. Acta* **2017**, *257*, 40−48.
(14) Li, S.; Yang, C.; Yin, Z.; Yang, H.; Chen, Y.; Lin, L.; Li, M.; Li, W.; Hu, G.; Ma, D. Wet-chemistry synthesis of cobalt carbide nanoparticles as highly active and stable electrocatalyst for hydrogen evolution reaction. *Nano Res.* **2017**, *10* (4), 1322−1328.
(15) Ma, X.; Li, K.; Zhang, X.; Wei, B.; Yang, H.; Liu, L.; Zhang, M.; Zhang, X.; Chen, Y. The surface engineering of cobalt carbide spheres through N, B co-doping achieved by room-temperature in situ anchoring effects for active and durable multifunctional electrocatalysts. *J. Mater. Chem. A* **2019**, *7*, 14904−14915.
(16) Huba, Z. J.; Carpenter, E. E. Size and phase control of cobalt−carbide nanoparticles using OH^- and Cl^- anions in a polyol process. *J. Appl. Phys.* **2012**, *111*, 07B529.
(17) McCrory, C. C.; Jung, S.; Peters, J. C.; Jaramillo, T. F. Benchmarking heterogeneous electrocatalysts for the oxygen evolution reaction. *J. Am. Chem. Soc.* **2013**, *135*, 16977−16987.
(18) Perdew, J. P.; Burke, K.; Ernzerhof, M. Generalized gradient approximation made simple. *Phys. Rev. Lett.* **1996**, *77* (18), 3865.
(19) Perdew, J. P.; Burke, K.; Ernzerhof, M. Generalized gradient approximation made simple. *Phys. Rev. Lett.* **1996**, *77*, 3865; *Phys. Rev. Lett.* **1997**, *78* (7), 1396.
(20) Hammer, B. H. L. B.; Hansen, L. B.; Nørskov, J. K. Improved adsorption energetics within density-functional theory using revised Perdew-Burke-Ernzerhof functionals. *Phys. Rev. B: Condens. Matter Mater. Phys.* **1999**, *59* (11), 7413.
(21) Man, I. C.; Su, H. Y.; Calle-Vallejo, F.; Hansen, H. A.; Martínez, J. I.; Inoglu, N. G.; Kitchin, J.; Jaramillo, T. F.; Nørskov, J. K.; Rossmeisl, J. Universality in oxygen evolution electrocatalysis on oxide surfaces. *ChemCatChem* **2011**, *3* (7), 1159−1165.
(22) Peterson, A. A.; Abild-Pedersen, F.; Studt, F.; Rossmeisl, J.; Nørskov, J. K. How copper catalyzes the electroreduction of carbon dioxide into hydrocarbon fuels. *Energy Environ. Sci.* **2010**, *3* (9), 1311−1315.
(23) Madsen, G. K.; Carrete, J.; Verstraete, M. J. BoltzTraP2, a program for interpolating band structures and calculating semi-classical transport coefficients. *Comput. Phys. Commun.* **2018**, *231*, 140−145.
(24) Wei, X.; Li, N.; Zhang, X. Co/CoO/C@B three-phase composite derived from ZIF67 modified with $NaBH_4$ solution as the electrocatalyst for efficient oxygen evolution. *Electrochim. Acta* **2018**, *264*, 36−45.
(25) Chen, Z.; Liu, L.; Chen, Q. One-pot template-free synthesis of urchin-like Co_2C/Co_3C hybrid nanoparticles. *Mater. Lett.* **2016**, *164*, 554−557.
(26) Kim, J. H.; Kawashima, K.; Wygant, B. R.; Mabayoje, O.; Liu, Y.; Wang, J.; Mullins, C. B. Transformation of a cobalt carbide (Co_3C) oxygen evolution pre-catalyst. *ACS Appl. Energy Mater.* **2018**, *1*, 5145−5150.
(27) Chen, I. H.; Wang, C. C.; Chen, C. Y. Fabrication and characterization of magnetic cobalt ferrite/polyacrylonitrile and cobalt ferrite/carbon nanofibers by electrospinning. *Carbon* **2010**, *48*, 604−611.
(28) Ma, K.; Liu, F.; Yuan, Y. F.; Liu, X. Q.; Wang, J.; Xie, J.; Cheng, J. P. CoO microspheres and metallic Co evolved from hexagonal α-$Co(OH)_2$ plates in a hydrothermal process for lithium storage and magnetic applications. *Phys. Chem. Chem. Phys.* **2018**, *20*, 595−604.
(29) Cheng, H.; Su, Y. Z.; Kuang, P. Y.; Chen, G. F.; Liu, Z. Q. Hierarchical $NiCo_2O_4$ nanosheet-decorated carbon nanotubes towards highly efficient electrocatalyst for water oxidation. *J. Mater. Chem. A* **2015**, *3*, 19314−19321.
(30) Petit, C.; Pileni, M. P. Cobalt nanosized particles organized in a 2D superlattice: synthesis, characterization, and magnetic properties. *J. Phys. Chem. B* **1999**, *103* (11), 1805−1810.
(31) Yang, W.; Liu, X.; Yue, X.; Jia, J.; Guo, S. Bamboo-like carbon nanotube/Fe_3C nanoparticle hybrids and their highly efficient catalysis for oxygen reduction. *J. Am. Chem. Soc.* **2015**, *137* (4), 1436−1439.
(32) Chung, D. Y.; Jun, S. W.; Yoon, G.; Kim, H.; Yoo, J. M.; Lee, K. S.; Kim, T.; Shin, H.; Sinha, A. K.; Kwon, S. G.; Kang, K.; Hyeon, T.; Sung, Y. E. Large-scale synthesis of carbon-shell-coated FeP nanoparticles for robust hydrogen evolution reaction electrocatalyst. *J. Am. Chem. Soc.* **2017**, *139* (19), 6669−6674.
(33) Shen, Y.; Zhou, Y.; Wang, D.; Wu, X.; Li, J.; Xi, J. Nickel−copper alloy encapsulated in graphitic carbon shells as electrocatalysts for hydrogen evolution reaction. *Adv. Energy Mater.* **2018**, *8* (2), 1701759.
(34) Mabayoje, O.; Dunning, S. G.; Kawashima, K.; Wygant, B. R.; Ciufo, R. A.; Humphrey, S. M.; Mullins, C. B. Hydrogen Evolution by Ni_2P Catalysts Derived from Phosphine MOFs. *ACS Appl. Energy Mater.* **2020**, *3* (1), 176−183.
(35) Kuznetsov, V. L.; Butenko, Y. V.; Chuvilin, A. L.; Romanenko, A. I.; Okotrub, A. V. Electrical resistivity of graphitized ultra-disperse diamond and onion-like carbon. *Chem. Phys. Lett.* **2001**, *336* (5−6), 397−404.
(36) Zhang, H.; Liang, C.; Liu, J.; Tian, Z.; Shao, G. The formation of onion-like carbon-encapsulated cobalt carbide core/shell nanoparticles by the laser ablation of metallic cobalt in acetone. *Carbon* **2013**, *55*, 108−115.
(37) Harris, V. G.; Chen, Y.; Yang, A.; Yoon, S.; Chen, Z.; Geiler, A. L.; Gao, J.; Chinnasamy, C. N.; Lewis, L. H.; Vittoria, C.; Carpenter, E. E.; Carroll, K. J.; Goswami, R.; Willard, M. A.; Kurihara, L.; Gjoka, M.; Kalogirou, O. High coercivity cobalt carbide nanoparticles processed via polyol reaction: a new permanent magnet material. *J. Phys. D: Appl. Phys.* **2010**, *43* (16), 165003.
(38) Carroll, K. J.; Huba, Z. J.; Spurgeon, S. R.; Qian, M.; Khanna, S. N.; Hudgins, D. M.; Taheri, M. L.; Carpenter, E. E. Magnetic properties of Co_2C and Co_3C nanoparticles and their assemblies. *Appl. Phys. Lett.* **2012**, *101* (1), 012409.
(39) Wiley, B.; Herricks, T.; Sun, Y.; Xia, Y. Polyol synthesis of silver nanoparticles: use of chloride and oxygen to promote the formation of single-crystal, truncated cubes and tetrahedrons. *Nano Lett.* **2004**, *4* (9), 1733−1739.
(40) Niessen, A. K.; De Boer, F. R. The enthalpy of formation of solid borides, carbides, nitrides, silicides and phosphides of transition and noble metals. *J. Less-Common Met.* **1981**, *82*, 75−80.
(41) Stevanović, V.; Lany, S.; Zhang, X.; Zunger, A. Correcting density functional theory for accurate predictions of compound enthalpies of formation: Fitted elemental-phase reference energies. *Phys. Rev. B: Condens. Matter Mater. Phys.* **2012**, *85* (11), 115104.
(42) Bate, L. C.; Leddicotte, G. W. *The radiochemistry of cobalt*. National Academy of Sciences: Washington, DC, USA, 1961; Vol. *3041*, DOI: 10.2172/4842901.
(43) Nørskov, J. K.; Bligaard, T.; Logadottir, A.; Kitchin, J. R.; Chen, J. G.; Pandelov, S.; Stimming, U. Trends in the exchange current for hydrogen evolution. *J. Electrochem. Soc.* **2005**, *152* (3), J23−J26.
(44) Betteridge, W. The properties of metallic cobalt. *Prog. Mater. Sci.* **1980**, *24*, 51−142.
(45) Ma, F. X.; Wu, H. B.; Xia, B. Y.; Xu, C. Y.; Lou, X. W. Hierarchical β-Mo_2C nanotubes organized by ultrathin nanosheets as a highly efficient electrocatalyst for hydrogen production. *Angew. Chem., Int. Ed.* **2015**, *54* (51), 15395−15399.

https://dx.doi.org/10.1021/acsaem.0c00321
ACS Appl. Energy Mater. 2020, 3, 3909−3918

(46) Lu, X. F.; Yu, L.; Zhang, J.; Lou, X. W. Ultrafine dual-phased carbide nanocrystals confined in porous nitrogen-doped carbon dodecahedrons for efficient hydrogen evolution reaction. *Adv. Mater.* **2019**, *31* (30), 1900699.
(47) Jiang, J.; Liu, Q.; Zeng, C.; Ai, L. Cobalt/molybdenum carbide@N-doped carbon as a bifunctional electrocatalyst for hydrogen and oxygen evolution reactions. *J. Mater. Chem. A* **2017**, *5* (32), 16929−16935.
(48) Zhao, X.; He, X.; Yin, F.; Chen, B.; Li, G.; Yin, H. Cobalt-molybdenum carbide@graphitic carbon nanocomposites: Metallic cobalt promotes the electrochemical hydrogen evolution reaction. *Int. J. Hydrogen Energy* **2018**, *43* (49), 22243−22252.

https://dx.doi.org/10.1021/acsaem.0c00321
ACS Appl. Energy Mater. 2020, 3, 3909−3918